Nonequilibrium Green's function study of phonon-dressed Auger transitions in superlattice infrared photodetectors

Nonequilibrium Green's function study of phonon-dressed Auger transitions in superlattice infrared photodetectors

Jesus Alberto Gonzalez Montoya,[1] Alberto Tibaldi,[1,*] Michele Goano,[1,2] and Francesco Bertazzi[1,2]

[1] *DET, Politecnico di Torino, Torino, Italy*
[2] *IEIIT-CNR, Torino, Italy*

(Received 29 July 2024; revised 11 November 2024; accepted 2 January 2025; published 23 January 2025)

Antimonide-based type-II superlattices represent a promising alternative to mercury cadmium telluride in infrared imaging applications. Among the original motivations for the development of type-II superlattices as a material system for infrared photodetectors is Auger engineering, the possibility of tailoring Auger processes to increase the "intrinsic" minority carrier lifetime at long wavelengths. We investigate Auger transitions in antimonide-based superlattices by means of a nonequilibrium Green's function model based on a multiband description of the electronic structure and a *GW* treatment of carrier-carrier interactions. As carrier-phonon interactions mediated by acoustic deformation potential and polar optical scattering are included by means of appropriate self-energies, the resulting *GW* Auger rates may be considered as "phonon-dressed." The spatial and spectral resolution afforded by the model provides a clear, graphical representation of the transitions contributing to the recombination process. A detailed study of Auger transitions in conventional and polytype superlattice absorbers demonstrates the effectiveness of the proposed approach for the design of Auger-suppressed infrared photodetectors. The calculated Auger coefficients are in good agreement with measurements extracted from pulsed threshold current densities of midwave infrared lasers with active regions realized with type-II quantum wells.

DOI: 10.1103/PhysRevApplied.23.014050

I. INTRODUCTION

The band structure flexibility of antimonide-based type-II superlattices (T2SLs) provides detection wavelength tunability over most of the infrared spectrum, but, crucially, also the possibility of suppressing Auger recombination to achieve lower dark currents and higher operating temperatures. Indeed, Auger engineering was one of the main motivations that led to the development of antimonide-based T2SLs as an alternative material system to the well-established infrared imaging technology based on bulk mercury cadmium telluride (HgCdTe) [1]. In the absence of Shockley-Read-Hall (SRH) recombination centers, Auger processes determine the longest attainable minority carrier lifetime [2], ultimately limiting detector performances. As the large effective ratios between electron and hole masses and the degeneracy of heavy- and light-hole bands allow energy and crystal momentum to be easily conserved for Auger transitions in HgCdTe alloys, several high-operating-temperature architectures including exclusion and extraction heterojunctions were proposed to suppress Auger mechanisms, by essentially reducing carrier densities below thermal equilibrium intrinsic values [3]. T2SLs offer a fundamental advantage over the HgCdTe material system, since Auger coefficients may be reduced at the material level by band-edge optimization (i.e., strategies that alter the electronic structure of the superlattice (SL) near the valence and conduction miniband edges) or final state optimization (i.e., the reduction of phase space for Auger transitions) [4].

Auger recombination is clearly not the only factor limiting the performance of infrared detectors. The presence of SRH recombination centers [1], compositional or structural disorder [5], and scattering-mediated carrier transport [6] may also play an important role especially in the case of narrow minibands, and it is perhaps for this reason that the full potential of Auger engineering has not yet been revealed. Nevertheless, experimental results encouragingly indicate reduced Auger coefficients in T2SLs. Room-temperature pump-probe experiments reported an Auger coefficient of 1.4×10^{-28} cm^6/s for a 9-μm band-gap InAs/InAsSb T2SL, a suppression of two orders of magnitude with respect to epilayers of InSb of comparable band gap [7]. Auger recombination in a long-wavelength infrared (LWIR) InAs/InAsSb T2SL with a cutoff wavelength of 11.5 μm measured by means of a time-resolved microwave reflectance technique was found to be approximately an order of magnitude smaller compared to coefficients in HgCdTe with the same band-gap energy over the 20–80 K temperature range [2].

*Contact author: alberto.tibaldi@polito.it

The interest in Auger-engineered T2SLs is not just limited to infrared photodetectors. A recent comparison of threshold current densities in midwave infrared (mid-IR) semiconductor lasers indicates that Auger recombination is substantially suppressed in type-II quantum wells (QWs) with respect to bulk mid-IR materials, since the degeneracy of the heavy- and light-hole subbands is lifted and the much lighter in-plane hole effective mass near the top of the valence band increases the threshold energy for Auger recombination at room temperature [8]. Band-engineered T2SLs are also attracting attention in the context of avalanche photodetectors , where optimal performance is achieved when the avalanche process (Auger generation) is unipolar, that is, dominated by either electrons or holes [9–11].

On the theoretical side, calculations of Auger coefficients in T2SLs are still incomplete and mostly limited to direct, phononless processes. Early Fermi-golden-rule calculations of minority carrier lifetimes in ideal InGaSb/InAs SLs predicted the suppression of Auger processes in p-type absorbers when the splitting of heavy- and light-hole bands exceeds the energy gap, thus limiting phase space for recombination transitions [12,13]. A later investigation by Grein addressed the possible impact of momentum relaxation due to the presence of compositional and structural disorder in T2SLs, as well as Fröhlich scattering with longitudinal optical phonons assisting the Auger transitions [14]. More recently, a comparative analysis of electroluminescence efficiency in type-I and type-II heterostructures based on III–V narrow-gap compounds showed that type-II band alignment has favorable properties in terms of Auger recombination coefficients due to the partial destructive interference of different tunneling-assisted recombination channels [15].

Direct (i.e., phononless) Auger coefficients in semiconductor nanostructures are usually computed by means of the first-order Fermi golden rule, while indirect phonon-assisted processes require second-order perturbation theory [16]. Although Fermi-golden-rule calculations provide useful information concerning the strength of the different recombination channels, they have to be included in a carrier transport model to obtain the relevant figures of merits. The study of Auger recombination cannot be entirely separated from a carrier transport analysis, as the excess energy resulting from the recombination process may promote carriers from the localized states to the extended, current-carrying states of the nanostructure, calling for a unified treatment of transport and recombination processes. As an example, we mention the complex role of Auger recombination in the efficiency droop observed in visible-light-emitting diodes, the decline of the internal quantum efficiency at high current levels: besides competing with radiative recombination processes, Auger mechanisms also provide an important contribution to leakage [17]. In T2SLs, carrier transport and Auger generation are intimately connected, as tunneling and phonon scattering provide the carriers the energy needed to overcome minigaps, thus enabling the impact ionization process [10].

On our way towards a simulation framework that treats carrier transport and recombination processes on an equal footing, we propose a nonequilibrium Green's function (NEGF) model for the calculation of Auger coefficients. Our previous studies have shown that the NEGF formalism is well suited to describing the different transport mechanisms in T2SLs, which range from miniband transport to Wannier-Stark hopping, depending on geometrical parameters, temperature, and the presence of built-in and/or applied electric fields [6,18]. Within the NEGF theory, Auger transition rates can be obtained from the interband polarizability and the screened Coulomb interaction at the level of the *GW* approximation [19]. *GW* schemes are widely used to describe the quasiparticle band structures and spectroscopic properties of extended and low-dimensional systems [20], but their application in the context of carrier transport is far less established, the treatment of carrier-carrier interactions usually being limited to the Hartree approximation through the self-consistent solution of Poisson's equation. Notable exceptions are *GW*-NEGF studies of relaxation processes in terahertz quantum cascade lasers [21], hot carrier transport in photoexcited quantum-well solar cells [22], and carrier-carrier interactions in single-walled carbon nanotubes [23]. In this work, we study Auger recombination in infrared SL absorbers by means of an NEGF model based on the *GW* formalism, within a multiband $k \cdot p$ description of the electronic structure.

Among different infrared imaging architectures, barrier photodetectors represent the most popular solution for materials with inherently short SRH lifetimes [1,24]. Barrier photodetectors are essentially *pn* devices in which the space charge region is limited within the wide band-gap barrier for majority carriers [25]. Since the focus of this work is on Auger transitions, we restrict our attention to the absorbing region of the detector, which is designed to remain approximately in flat band at operating conditions, with the applied bias mostly dropping across the barrier layer to avoid large depletion dark currents. As *GW* calculations are feasible only for a small fraction of the SL absorber, we impose open boundary conditions with periodic SL contacts to avoid finite-size effects. Following the conventional quasiequilibrium assumption adopted in Fermi-golden-rule calculations of Auger coefficients in QWs, excess populations of electrons and holes are obtained by splitting the Fermi levels of the SL contacts, thus mimicking the optical illumination of the sample.

II. THEORY AND RESULTS

The numerical discretization of the NEGF model is based on a multiband $k \cdot p$ description of the electronic

structure for zincblende crystals [6], which includes the first conduction band, heavy-hole, light-hole, and spin-orbit splitoff bands. The bulk Hamiltonian can be block-diagonalized with respect to the spin components, that is, the 8×8 Hamiltonian decouples into two 4×4 blocks, and the energy dispersion becomes isotropic in the plane perpendicular to the c axis [6]. Assuming one-dimensional layered structures, Green's functions and self-energies are expressed in terms of first-order Lagrange polynomials $t_i(z)$ to expand the slowly varying envelopes describing the mixing of the lattice-periodic functions at every position in the symmetry-broken direction z, and plane waves in the translationally invariant directions $\underline{r} = (x, y)$,

$$\phi_{\underline{k}\alpha}(\underline{r}, z) = \frac{1}{\sqrt{\mathcal{A}}} e^{i\underline{k}\cdot\underline{r}} u_a(\underline{r}, z) t_i(z), \tag{1}$$

where $\alpha = (a, i)$ is a compound index combining indices a for band and i for space, $u_a(\underline{r}, z)$ are the zone-center Bloch functions, and $\mathcal{A}$ is the normalization area. In full matrix notation, the steady-state (Fourier-transformed) Dyson and Keldysh equations read [26–28]

$$G^R(\underline{k}, E) = [EM - H(\underline{k}) - \Sigma^R(\underline{k}, E)]^{-1}, \tag{2a}$$

$$G^{\lessgtr}(\underline{k}, E) = G^R(\underline{k}, E)\Sigma^{\lessgtr}(\underline{k}, E)G^A(\underline{k}, E), \tag{2b}$$

in which a contravariant representation is used for Green's functions and a covariant representation for self-energies, the two representations being related by the overlap matrix M. Coupling to acoustic and polar optical phonons is included by means of the self-energy [6]

$$\begin{aligned}[\Sigma^{\lessgtr}_{\text{ep}}(\underline{k}, E)]_{\alpha\beta} = \sum_{\underline{q}, q_z} |U(\underline{q}, q_z)|^2 e^{iq_z(z_i - z_j)} \\ \times \{n_{\text{ph}} M G^{\lessgtr}(\underline{k} - \underline{q}, E^{\mp}) M \\ + [n_{\text{ph}} + 1] M G^{\lessgtr}(\underline{k} - \underline{q}, E^{\pm}) M\}_{\alpha\beta},\end{aligned} \tag{3}$$

where $\alpha = (a, i)$ and $\beta = (b, j)$ are compound indices including band and nodal indices, n_{ph} is the phonon number, $\hbar\omega_{\text{ph}}$ is the phonon energy, and $E^{\pm} = E \pm \hbar\omega_{\text{ph}}$. We assume an equilibrium population of bulk phonons with transverse and longitudinal wave vectors q and q_z, respectively. Acoustic scattering is treated within the elastic approximation and polar optical phonons are assumed dispersionless. Material parameters and expressions of the coupling constants U for acoustic deformation potential and polar optical scattering are provided in [6]. Neglecting energy renormalizations, the retarded component of the carrier-phonon self-energy is computed as $\Sigma^R_{\text{ep}} = (\Sigma^{>}_{\text{ep}} - \Sigma^{<}_{\text{ep}})/2$ [26].

While infrared SL absorbers are usually several micrometers long to absorb a significant fraction of the incident light, multiband GW calculations are possible only for a few SL periods. In order to avoid finite-size effects imposed by constraints on the computational domain, we introduce a periodic boundary condition that mimics the local density of states (LDOS) injected by semi-infinite SLs. A preliminary step towards the calculation of such boundary self-energy is the determination of the complex band structure of the SL. The derivation is similar to the bulk case for a tight-binding description of the electronic structure [30], provided that we identify the "principal layers" (defined in [30] as the minimal group of atomic planes with nearest-neighbor interactions) with the $k \cdot p$ atomic functions associated to a given node of the mesh, and the "superlayer" (i.e., the smallest collection of principal layers that form the unit cell of the solid) with the nodes of the SL unit cell. Assuming nearest-nodes interactions, the Schrödinger equation for a single SL unit cell reads in block matrix notation

$$h_{N+1,N}F_N^{(n-1)} + h_{1,1}F_1^{(n)} + h_{1,2}F_2^{(n)} = 0, \tag{4a}$$

$$h_{i,i-1}F_{i-1}^{(n)} + h_{i,i}F_i^{(n)} + h_{i,i+1}F_{i+1}^{(n)} = 0, \quad \text{for } i = 2, \ldots, N-1, \tag{4b}$$

$$h_{N,N-1}F_{N-1}^{(n)} + h_{N,N}F_N^{(n)} + h_{N,N+1}F_1^{(n+1)} = 0, \tag{4c}$$

where N is the number of nodes in an SL unit cell, $F_i^{(n)}$ is a column array of size $B = 8$, which includes the $k \cdot p$ expansion coefficients of the wave function computed at node i in the nth period, and $h_{i,j} = h_{i+N,j+N} = EM_{i,j} - H_{i,j}$ is the $B \times B$ block of the Hamiltonian matrix connecting nodes i and j. Wave vector arguments have been dropped for clarity. Looking for Bloch waves of the form $F^{(n)} = F^{(n-1)}e^{ik_z d}$, where d is the periodicity of the SL, and choosing $n = 0$ as the reference period, we find the following generalized eigenvalue problem of size $BN \times BN$: $(F \equiv F^{(0)})$

$$\begin{bmatrix} 0 & \cdots & \cdots & 0 & h_{N+1,N} \\ & \ddots & \ddots & \ddots & \\ 0 & \cdots & h_{N-1,N-2} & h_{N-1,N-1} & h_{N-1,N} \\ 0 & \cdots & 0 & h_{N,N-1} & h_{N,N} \end{bmatrix} \begin{bmatrix} F_1 \\ F_2 \\ \vdots \\ F_N \end{bmatrix} = e^{ik_z d} \begin{bmatrix} -h_{1,1} & -h_{1,2} & \cdots & 0 \\ \vdots & & \vdots & \vdots \\ 0 & 0 & \cdots & 0 \\ -h_{N,N+1} & 0 & \cdots & 0 \end{bmatrix} \begin{bmatrix} F_1 \\ F_2 \\ \vdots \\ F_N \end{bmatrix}. \tag{5}$$

Having computed the group velocity of the $2B$ nontrivial eigensolutions of (5) with the Feynman-Hellmann

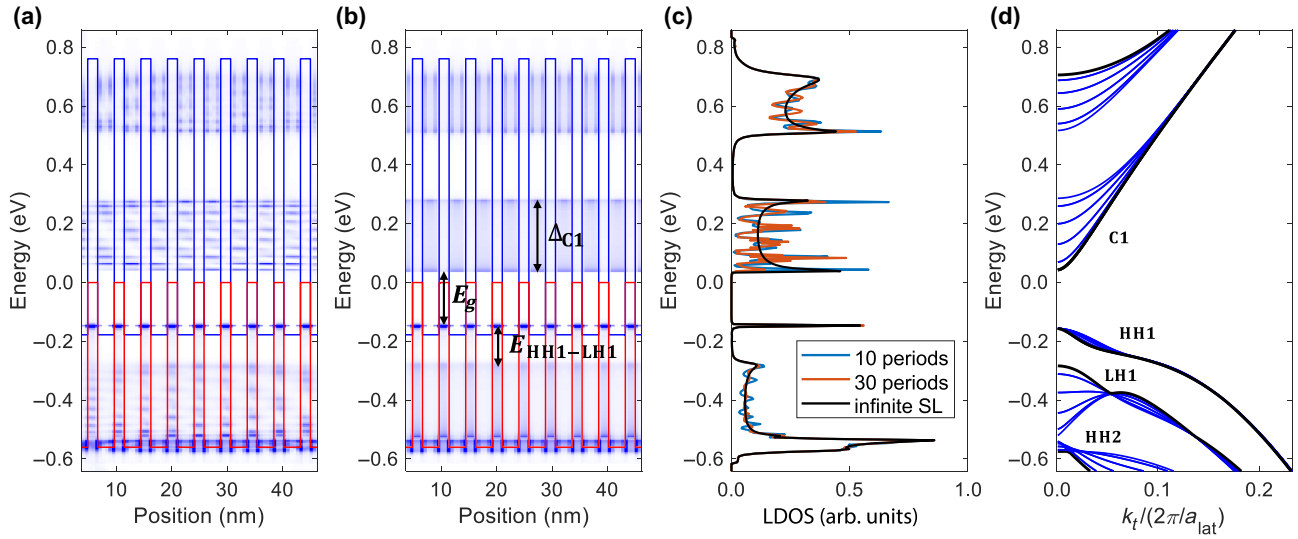

FIG. 1. Local density of states (LDOS) shown for $\underline{k} = 0$ of a 10-period T2SL consisting in the alternating sequence of 3 nm InAs and 1.8 nm GaSb layers, computed at $T = 200$ K with (a) bulk contacts and (b) superlattice (SL) contacts. (c) Cuts of the LDOS shown at $z = 28$ nm for a different number of periods, revealing ripples related to finite-size effects persisting up to a large number of periods. (d) $k \cdot p$ subband structure of the T2SL plotted versus normalized wave vectors along the in-plane direction (a_{lat} is the lattice constant). The in-plane dispersion for $k_z = 0$ is shown in black, while the blue curves are for equally spaced values of k_z up to the mini-Brillouin-zone boundary π/d (d is the SL period). Luttinger parameters used in the calculation of the electronic structure are from Ref. [29].

theorem, we arrange the B left-going (propagating or decaying) waves in the columns of matrix $U^<$, and the corresponding B right-going solutions in $U^>$. From the surface Green's function of the left-contacted Hamiltonian (i.e., the Hamiltonian obtained neglecting all couplings to the right), we find the following nonzero (block) entry of the left boundary self-energy:

$$[\Sigma^R_{\text{SL}}]_{1,N} = -h_{N+1,N} U^<_N (\Lambda^<)^{-1} (U^<_N)^{-1}, \tag{6}$$

where $U^<_N$ is the subblock of $U^<$ corresponding to node N, and $\Lambda^<$ is a diagonal matrix whose diagonal elements are the propagation factors $e^{ik^<_z d}$ of the left-traveling solutions. A similar procedure provides the boundary self-energy of the right (SL) contact

$$[\Sigma^R_{\text{SL}}]_{N,1} = -h_{N,N+1} U^>_1 (\Lambda^>)(U^>_1)^{-1}. \tag{7}$$

Figure 1 compares the LDOS of a 10-period SL, computed with the conventional open boundary conditions for bulk contacts (a), and with the SL boundary self-energy (b). The speckled LDOS of the finite SL indicates the presence of interacting states just beginning to take the shape of a miniband, but not yet merging into a continuum of states. The ripples in the vertical cuts of the LDOS, shown for different SL lengths in Fig. 1(c), appear more evident for the conduction minibands. Finite-size artifacts are clearly visible for the 10-period SL (blue line), and persist for the largest structure considered here (30 periods, red line). In the central region of the SL, the LDOS eventually converges to the LDOS of the infinite SL (black line) as the number of periods is further increased. The large number of periods needed to approximate the infinite SL, as well as the inevitable border effects introduced by the conventional "bulk" boundary self-energy, motivated us in the development of the SL self-energy described above. Completing the information of the LDOS is the subband dispersion in the transverse plane k [Fig. 1(d)], computed by solving the $k \cdot p$ Schrödinger equation with Bloch boundary conditions [31]. The in-plane dispersion for $k_z = 0$ is shown in black, while the blue curves are for equally spaced values of k_z up to the mini-Brillouin-zone boundary π/d. The HH1 subband appears almost dispersionless along the growth direction, which is consistent with the weakly interacting states that appear in the LDOS at an energy slightly above -0.2 eV. A small dispersion due to band mixing effects can be observed in the subband plot for intermediate in-plane wave vectors [32], but the effect is not visible in the LDOS, which is shown for normal incidence. The narrowness of the HH1 miniband does have important consequences for the transport of holes, which appears to be thermally activated by hopping processes [2], in agreement with temperature-dependent mobility studies [5,6]. As we will see, the strong confinement of carriers in a miniband also has important effects on the Auger recombination rate.

With the computational domain now limited to just few SL periods, we compute the GW self-energy encoding

carrier-carrier interactions as [22,33]

$$[\Sigma^{\lessgtr}_{GW}(\underline{k},E)]_{\alpha\beta} = \mathrm{i}\sum_{\underline{q}}\sum_{\delta\gamma}\int\frac{\mathrm{d}E'}{2\pi}G^{\lessgtr}_{\delta\gamma}(\underline{k}+\underline{q},E+E')W^{\gtrless}_{\alpha\gamma\beta\delta}(\underline{q},E'). \quad (8)$$

The lesser and greater components of the effective carrier-carrier interaction are given by

$$W^{\lessgtr}(\underline{q},E') = W^{R}(\underline{q},E')\Pi^{\lessgtr}(\underline{q},E')W^{A}(\underline{q},E'), \quad (9)$$

where Π is the polarization function

$$\Pi^{\lessgtr}_{\alpha\beta\delta\gamma}(\underline{q},E') = -\mathrm{i}\sum_{\underline{k}'}\int\frac{\mathrm{d}E''}{2\pi}G^{\lessgtr}_{\alpha\beta}(\underline{k}',E'')G^{\gtrless}_{\delta\gamma}(\underline{k}'-\underline{q},E''-E'). \quad (10)$$

In order to reduce the computational burden, we approximate the retarded and advanced components of the effective Coulomb interaction by the statically screened expression [22,34,35]

$$W^{R,A}_{\alpha\beta\delta\gamma}(\underline{q},E') = \frac{\mathrm{e}^2}{2\varepsilon\varepsilon_0\mathcal{A}}\iint\mathrm{d}z\mathrm{d}z' \times\phi^{*}_{\underline{k}\alpha}(z)\phi^{*}_{\underline{k}'\beta}(z')\frac{e^{-\sqrt{q_0^2+q^2}|z_i-z'_j|}}{\sqrt{q_0^2+q^2}}\phi_{\underline{k}\delta}(z')\phi_{\underline{k}'\gamma}(z), \quad (11)$$

where $\underline{q}=\underline{k}-\underline{k}'$, ε is the Lindhard dielectric function, q_0 is the inverse screening length, and $\mathcal{A}$ is the normalization area. As the LDOS is mainly modified by intraband scattering processes (carrier-phonon interactions), phonon scattering times being several orders of magnitude shorter than Auger lifetimes, we include the *GW* self-energy only in the last few self-consistent Born iterations to achieve current conservation. Upon convergence of the self-consistent loop, we find from the NEGF version of the continuity equation [36], and the additive property of the self-energies, the (net) Auger recombination rate

$$\mathcal{R}_{\mathrm{Aug}} = \frac{1}{\mathcal{A}}\sum_{\underline{k}}\int\frac{\mathrm{d}E}{2\pi\hbar}2\mathbb{R}\mathrm{e}\{\mathrm{Tr}[\Sigma^{>}_{GW}G^{<}-\Sigma^{<}_{GW}G^{>}]\}, \quad (12)$$

where the trace is over finite-element degrees of freedom, and the energy integral is carried out over the conduction band only. Within the multiband description of the electronic structure considered here, electron and hole states may mix in spatial and energy coordinates. For example, in interband cascade infrared photodetectors , electron and hole minibands are intentionally aligned to enable interband tunneling between adjacent stages [6]). However, in the flat-band conditions, electron and hole states are always unambiguously defined, so that the different Auger processes can be distinguished by performing the energy integration in (8)–(10) over the relevant bands. For example, electron-initiated (*eeh*) or hole-initiated (*hhe*) processes are selected by limiting the energy integral in the polarization function (10) to the conduction or valence bands, respectively. Since carrier-phonon interactions are included in self-consistent procedure for the calculation of the Green's functions, the resulting Auger recombination rates may be considered as "phonon-dressed." Using the unperturbed (i.e., noninteracting) equilibrium form of the lesser and greater Green's functions [36], it can be shown that (12) reduces to the conventional Fermi-golden-rule expression for the direct (i.e., phononless) Auger process. One of the unique features of NEGF is the spatial and spectral resolution afforded by the method: ignoring the integral over energy in (12), as well as the integral over space implied in the trace operator, we find energy- and spatially resolved Auger rates, which are shown in Fig. 2 for different SLs. Blue and red shades in the central period of the SL represent in- and out-scattering for electrons, respectively; gray stripes in the adjacent periods represent the LDOS computed for normal incidence. The contact Fermi levels were computed from the neutrality condition, assuming a background doping level of 10^{17} cm^{-3}, and photoexcited carrier densities of 10^{15} cm^{-3}, which corresponds to a low-injection condition. All calculations were performed at 200 K, when the intrinsic concentration is still negligible with respect to the doping density, so that carrier statistics favors *eeh* or *hhe* Auger processes in *n*- or *p*-type materials, respectively.

Having defined the recombination current J as

$$J = \mathrm{e}\mathcal{R}_{\mathrm{Aug}}, \quad (13)$$

the convergence of the *GW* iteration scheme is monitored by computing the residual error $\delta J_k = J_k - J_{k-1}$ as a function of the self-consistent Born approximation iteration k; see Fig. 3. Depending on the level of confinement of the SL, several tens of iterations may be needed to achieve current conservation.

The results for the reference SL considered in Fig. 1 are shown in Figs. 2(a) and 2(e) for *n*- and *p*-type doping, respectively. Arrows connecting full circles (occupied states) with empty circles (free states) help to identify the nature of the process (*eeh* or *hhe*). In the *n*-doped structure, electrons in miniband C1 recombine with holes in miniband HH1, while partner electrons in C1 are promoted to higher states just above the upper edge of the same miniband, as the effective gap of the SL is comparable with the width of C1. In analogy with Auger recombination in bulk semiconductors, we may classify this Auger process as intraminiband (C2 is not involved

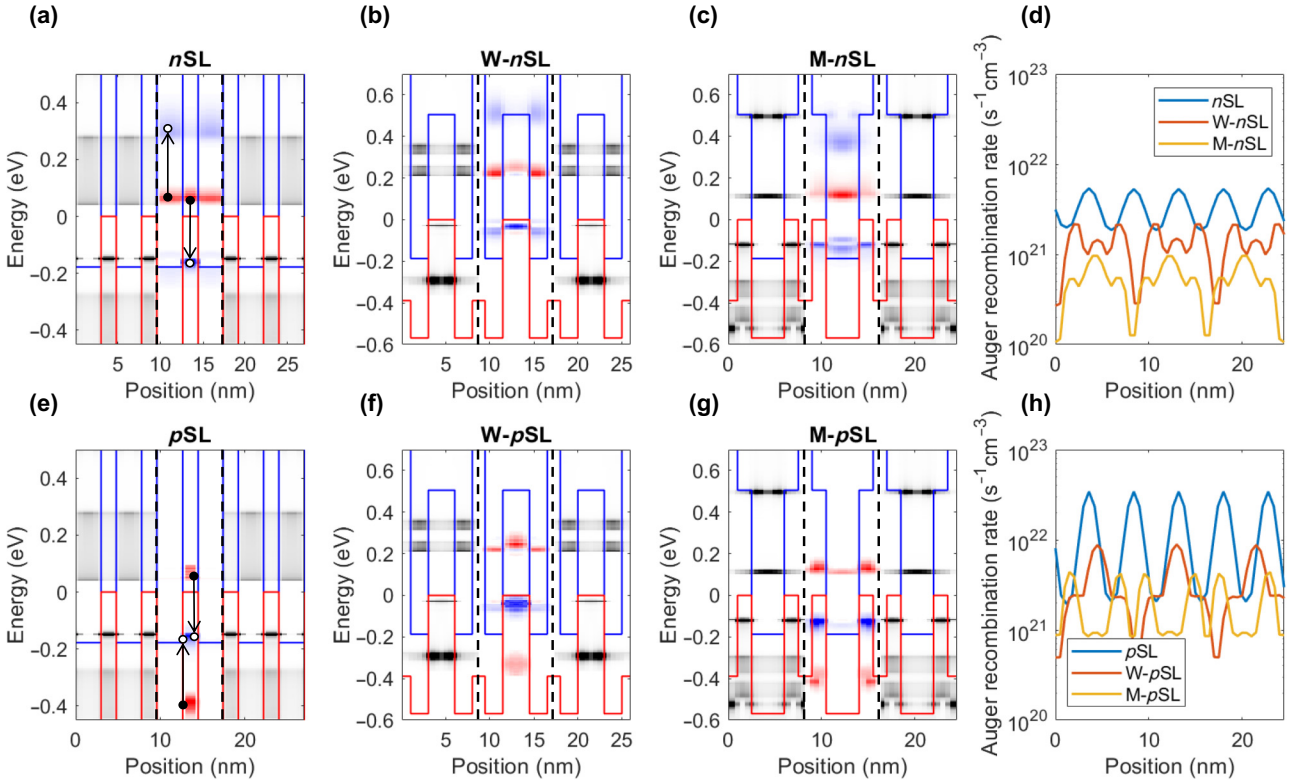

FIG. 2. Auger recombination rates calculated as a function of position and energy for the reference SL and the W- and M-structured SLs (color maps). All SLs have a uniform doping concentration of 10^{17} cm^{-3} (n-type in the upper panels, p-type in the lower panels), and are designed to have the same effective gap. Blue and red lines represent the conduction and valence band edges, respectively. Blue shades correspond to net in-scattering of electrons, while red shades correspond to net out-scattering. Arrows connecting full circles (occupied states) with empty circles (free states) are shown for the reference SL as a guide for the eye. The spectral recombination rates are shown only for the center period (the SL section within the dashed lines), periodicity being understood. Gray shades in the adjacent periods, on both sides of the center period, represent the LDOS evaluated for normal incidence, showing the spectral location of the minibands. The spectral and spatial resolution afforded by the NEGF formalism provides a useful graphical tool to design Auger-suppressed absorbers: scattering regions that do not overlap with the LDOS are indicative of less probable transitions as the exchange of a finite wave vector $\underline{q}$ is required to reach the final states. The energy-integrated Auger rates are displayed in (d) and (h) for n- and p-type structures, respectively. A photoexcited carrier concentration of 10^{15} cm^{-3} is imposed in all structures by splitting the Fermi levels of the contacts. All calculations were performed at 200 K.

as it is beyond the energy range of the figure). Comparing the Auger scattering rates out of C1 (red shades) with the LDOS shown in Fig. 1, one can notice the absence of an Auger threshold, the minimum energy from the miniband edge an electron must possess to initiate a recombination process. The appearance of thresholdless and quasithresholdless processes resulting in a weak, power-law temperature dependence of the direct (i.e., phononless) Auger rate, was first reported in narrow QWs [37,38], and was attributed to quantum confinement, which lifts the constraints imposed by momentum conservation. A similar effect was reported for phonon-assisted transitions in wide-band gap materials, as the participation of phonons allows carriers lying at the band edge to contribute to the recombination process [39]. In T2SLs, the enhancement of the Auger rate associated to the elimination of the threshold due to momentum transfer to heterointerfaces and phonons may be compensated by the spatial separation of electrons and holes, resulting in spatially indirect recombination processes. Indeed, although the downward "recombination" transitions (the ones that cross the effective gap) are localized in the GaSb layers, where the holes are confined, the accompanying transitions that generate Auger-excited electrons are mostly restricted to the InAs layers, making the overall process spatially indirect. On the other hand, *hhe* processes in the p-type SL appear more spatially direct [see Fig. 2(e)], which shows C1-HH1 transitions across the gap, accompanied by HH1-LH1 transitions in the valence minibands, with all the particles involved sitting in the GaSb layers. In this case, energy conservation requires the processes to be interminiband.

Since the alternating sequence of electron and hole confinement layers in long-period T2SLs leads to a reduction of the absorption coefficient [40], several polytype SLs

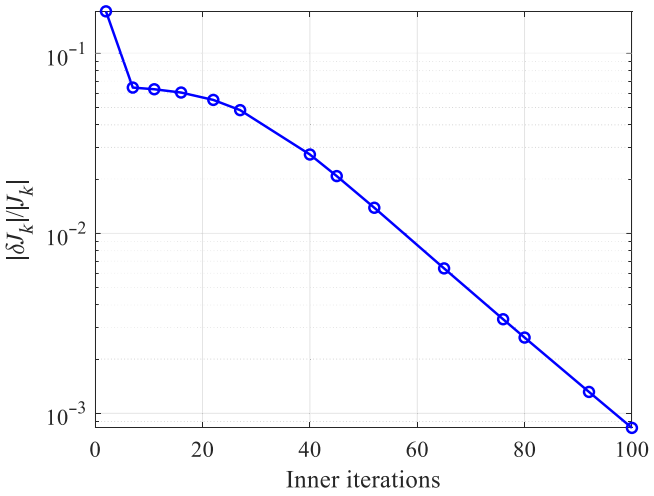

FIG. 3. Evolution of the relative residual error as a function of the number of self-consistent Born approximation iterations, computed for the reference *n*-type SL in Fig. 2(a). After 100 self-consistency iterations, when the relative residual error is less than 10^{-3}, the recombination current within the SL is approximately conserved.

with improved oscillator strengths have been considered as alternative materials for medium- and long-wavelength IR photodetectors [41–44]. Among them are W-structured T2SLs (W-SLs), originally proposed to increase the gain in mid-IR lasers [8,45], and M-structured type-II superlattices (M-SLs), introduced as alternative infrared materials in [46]. W-SLs are named after their characteristic W-shaped band-gap alignment in a single SL period, which includes two InAs electron QWs (the two pointy tips at the bottom of the letter "W") placed on both sides of a $Ga_{0.7}In_{0.3}Sb$ hole QW, and two AlSb barriers (the two outward strokes of the letter); see Fig. 2(b). The purpose of W-SLs is to confine the electron wave functions symmetrically on both sides of the hole well, increasing the electron-hole overlap, while still allowing miniband transport. M-SLs are formed by introducing the AlSb barriers in the middle of the GaSb layers of a binary InAs/GaSb SL. The resulting M-shaped alignment [see Fig. 2(c)] is easier to realize due to the small lattice mismatch between AlSb and GaSb and the common antimony atom. Layer thicknesses of the polytype SLs have been chosen to obtain the same effective band gap of the reference structure: the W-SL period consists of 1.5 nm AlSb, 2 nm InAs, 3 nm $Ga_{0.7}In_{0.3}Sb$, 2 nm InAs, while the M-SL sequence is 1.5 nm AlSb, 1.5 nm $Ga_{0.7}In_{0.3}Sb$, 3.5 nm InAs, 1.5 nm $Ga_{0.7}In_{0.3}Sb$. In conventional T2SLs, especially in the LWIR spectral region, electrons tend to be delocalized in a wide miniband, while holes are weakly coupled. In both the W and M configurations, conduction and valence minibands have comparable widths, which is indicative of a more symmetric confinement of the two carrier species; see Fig. 2.

TABLE I. Auger coefficients of the SLs investigated in Fig. 2, in units of cm^6/s.

	SL	W-SL	M-SL
C_{eeh}	1.751×10^{-28}	1.082×10^{-28}	4.797×10^{-29}
C_{hhe}	2.784×10^{-28}	2.067×10^{-28}	1.787×10^{-28}

The energy-integrated recombination rates of all structures are compared in Figs. 2(d) and 2(h) for the *n*- and *p*-type doping, respectively. A significant suppression of Auger recombination can be observed in W-SLs (red lines) and M-SLs (yellow lines) compared to the reference structure (blue lines). The spatial profile of the Auger rates has the periodicity of the SL, as expected in the absence of border effects. The reduction of the Auger rates in the *n*-doped W- and M-SLs may be attributed to the large transverse momenta exchanged in *eeh* transitions, as can be observed from the lack of overlap between the gray shades representing the LDOS and the blue spots that represent the in-scattering of the excited electrons; see Figs. 2(b) and 2(c). The suppression of C_{hhe} in the *p*-type structures is less remarkable, as the final states reached by the excited holes are partially overlapping with the valence minibands (HH2 in the W-SL, and LH1 in the M-SL); see Figs. 2(f) and 2(g). In all the structures considered, a higher recombination is consistently observed for *p*-type SLs. The relevance of *hhe* transitions (Auger 7 in the literature of narrow-gap semiconductors) in *p*-type LWIR SLs, notwithstanding the splitting of HH and LH subbands, which should be more effective for long wavelengths, was recently noted in [47].

Considering the SL as a bulk material with an artificial periodicity, and assuming that in the low- injection conditions considered here phase-space filling effects are negligible [48], we define the electron- and hole-initiated Auger coefficients of the SL from $R_{eeh} = C_{eeh}n^2p$ and $R_{hhe} = C_{hhe}np^2$, respectively, where n and p are the average electron and hole densities. The resulting Auger coefficients are reported in Table I.

In order to investigate the dependence of the Auger coefficients on geometrical parameters, we perform a study of the Auger coefficients as a function of the thickness of the InAs and GaSb layers, see Fig. 4. Also shown for reference are the corresponding profiles of the effective gap E_g (solid black line), the width of the conduction miniband Δ_{C1} (blue circles), the minigaps in the valence band (red symbols), and the most probable transition energies E_{eeh}, E_{hhe} for *eeh* and *hhe* processes, respectively (dashed lines).

As the thickness t_{InAs} of the InAs layers is increased, the conduction miniband shifts to lower energies, significantly reducing E_g, thus also increasing the Auger coefficients for both doping polarities. The most probable transition energies E_{eeh} and E_{hhe} remain larger than E_g by

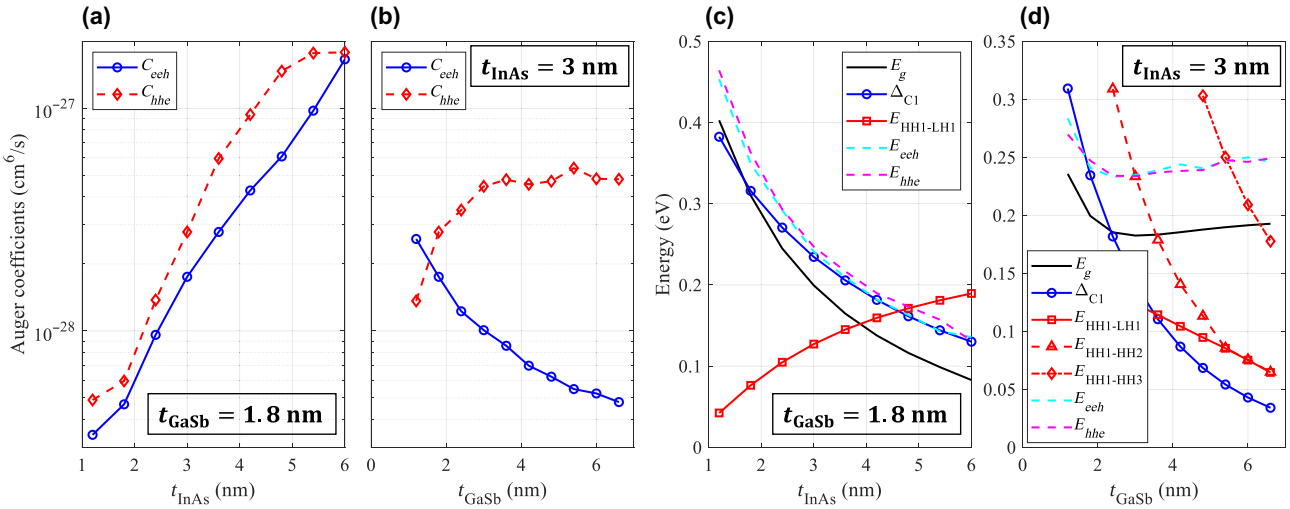

FIG. 4. (a),(b) Auger coefficients C_{eeh} and C_{hhe} as a function of the thickness of the InAs and GaSb layers. The corresponding effective band gaps E_g, conduction miniband widths Δ_{C1}, minigaps $E_{\mathrm{HH1\text{-}LH1}}$, $E_{\mathrm{HH1\text{-}HH2}}$, $E_{\mathrm{HH1\text{-}HH3}}$, and the most probable transition energies E_{eeh} and E_{hhe} (dashed lines) are reported in (c),(d). All calculations were performed at 200 K.

approximately 50 meV. Inspection of Fig. 2 reveals that this excess energy should not be interpreted as a threshold (phonon-induced tail states within the effective gap do contribute to Auger recombination), but rather it can be attributed to the spectral distribution of the electrons in C1, which peaks slightly above the miniband edge. The resulting increase of the average transition energies also explains why the relevant band resonances for Auger processes are not exactly observed at the intersection of minigaps with the effective gap. No significant features can be observed in C_{hhe} when the resonant condition $E_{\mathrm{HH1\text{-}LH1}} = E_g$ ($t_{\mathrm{InAs}} = 3.6$ nm) is reached, but a saturation of C_{hhe} due to momentum-conservation constraints appears at $E_{\mathrm{HH1\text{-}LH1}} = E_{hhe}$ ($t_{\mathrm{InAs}} = 4.8$ nm), when the *most probable* transitions in the valence band are restricted within the HH1 miniband. A similar effect can be observed for *eeh* processes if t_{GaSb} is changed from 1.8 nm to 1.2 nm. Thinner GaSb layers in the SL result in a wider conduction miniband C1, so that the condition $\Delta_{C1} = E_{eeh}$ is now reached within the investigated parameter range at $t_{\mathrm{InAs}} = 4.2$ nm, leading to a saddle point in C_{eeh}, despite the monotonic decrease of the effective gap; see Fig. 5. When the thickness t_{GaSb} of the GaSb layers is increased, the HH1 miniband remains almost unchanged, close to the valence band edge of GaSb, save for a negligible upward shift, thus slightly reducing the effective band gap. More importantly, the conduction miniband becomes narrower, which leads to a monotonic decrease of C_{eeh} [see Fig. 4(b)], as energy-conserving transitions involve increasingly larger qs in the transverse plane. On the other hand, C_{hhe} is mostly unaffected by the shrinking of C1, since only the lower, populated fraction of the miniband contributes to the recombination process. So, C_{hhe} initially increases due to the reduction of the effective gap, and then becomes almost constant at larger values of t_{GaSb}. At $t_{\mathrm{GaSb}} = 5.4$ nm, a small resonance in C_{hhe} is observed when $E_{\mathrm{HH1\text{-}HH3}}$ equals E_{hhe}. The absence of significant features in C_{hhe} may be attributed to the shift of miniband HH2 towards the valence band edge as t_{GaSb} is increased, while LH1 moves only slightly downwards, so that the two minibands are superimposed near the resonance $E_{\mathrm{HH1\text{-}HH2}} = E_{hhe}$ ($t_{\mathrm{GaSb}} = 3.0$ nm). When the next resonance $E_{\mathrm{HH1\text{-}HH3}} = E_{hhe}$ is reached at $t_{\mathrm{GaSb}} = 5.4$ nm, HH3 also overlaps with LH1. We conclude that no significant features can be observed in C_{hhe} since the two resonances are masked by the presence of HH1-LH1 transitions for any value of t_{GaSb} in the range considered. The relative insensitivity of the Auger rates with respect to band structure details was already observed in experimental measurements of Auger rates in type-II QWs, which found that *hhe* processes can indeed be substantial, but failed to find any systematic correlation with specific valence intersubband alignments relative to the energy gap [8,49]. The lack of band-related features in the Auger rates was attributed to the wide diversity of transitions that can occur, in conjunction with the broadening of the states by compositional and structural nonuniformities in the QWs. In addition to inhomogeneous broadening (not accounted for in our calculations), it should also be mentioned that energy and momentum conservation rules are somewhat blurred when Auger processes are dressed by phonons.

Finally, Fig. 6 compares the Auger coefficients computed with NEGF (solid blue and red lines for *eeh* and *hhe* processes, respectively), with experimental results (magenta circles) extracted from room-temperature pulsed threshold current densities of type-II interband cascade lasers (ICLs) with emitting wavelengths between 2.8 and 6.2 μm [8,50]. Since the ICLs under study were designed

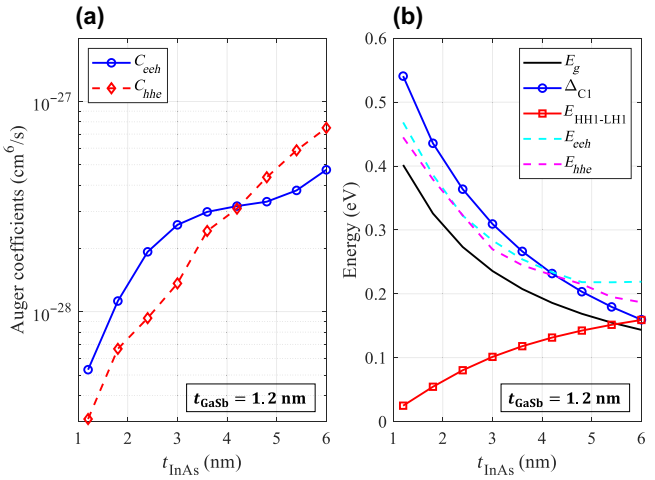

FIG. 5. (a) Auger coefficients C_{eeh} and C_{hhe} as a function of the thickness of the InAs layer, with a fixed GaSb thickness of 1.2 nm. (b) The corresponding effective band gap E_g, conduction miniband width Δ_{C1}, minigap $E_{HH1\text{-}LH1}$, and the most probable transition energies E_{eeh} and E_{hhe} (dashed lines).

to have nearly equalized electron and hole densities to optimize device performance, the experimental Auger coefficients presented in [8] can be compared with $C_{tot} = C_{eeh} +$

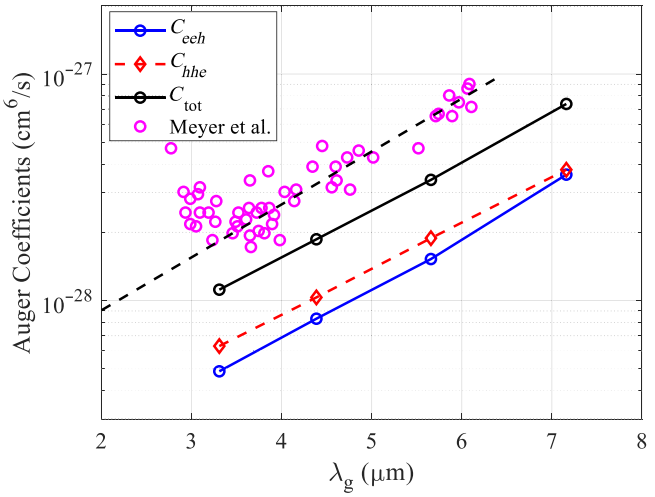

FIG. 6. Auger coefficients C_{eeh} and C_{hhe} computed with the NEGF approach at $T = 300$ K as a function of the SL cutoff wavelength, and the experimental three-dimensional Auger coefficients reported in [8] (magenta circles). The measurements, which represent the most complete Auger data for interband cascade lasers with type-II, W-shaped quantum wells , were extracted from pulsed thresholds at room temperature. The scattering of the experimental values is due to the variety of active QWs realized over a period of 11 years [8]. The interpolating dashed black line, used as a guide for the eye, is remarkably in agreement with the calculated total Auger coefficient $C_{tot} = C_{eeh} + C_{hhe}$ (solid back line) including both electron- and hole-initiated processes, which may be defined for structures with balanced populations of electrons and holes.

C_{hhe} (black solid line). The agreement between C_{tot} and the black dashed line (a guide for the eye for the experimental data) is satisfactory considering the sophisticated extraction procedure of the Auger coefficients from the lasing threshold, which requires accurate models for internal efficiencies, optical confinement factors, modal gains, and an unambiguous definition of the normalization length for the spatial extent of the carriers' confinement region [8]. Moreover, evidence from carrier-rebalancing studies [51] suggests that the Auger rates for *eeh* and *hhe* have comparable strengths in the 3–4 μm range, in agreement with the present calculations.

III. CONCLUSION

By means of an NEGF solver based on a multiband description of the electronic structure, we have described carrier-carrier interactions in T2SLs within a self-consistent *GW* approximation. The spectral and spatial resolution of the method provides insight into the mechanisms that limit Auger transitions in SL absorbers for infrared photodetectors. All the calculations presented in this work are performed for T2SLs in flat-band conditions, which apply, for example, to the absorbing region of a barrier photodetector. The extension of this analysis to other detector architectures (consider, for example, an SL absorber embedded within a reverse-biased *pn* junction) requires the self-consistent solution of Poisson's equation to account for space-charge effects (the periodic boundary self-energy proposed in this work is applicable to any SL photodetector with arbitrary applied or built-in electric fields, provided that the "device" region under study is terminated on both sides with semi-infinite equipotential SLs). This work represents a preliminary step towards an NEGF model in which intraband and interband self-energies are computed self-consistently, which would provide a simulation framework able to treat carrier transport and recombination processes on equal footing for the accurate assessment of minority carrier diffusion lengths, collection efficiencies, and multiplication gains in highly nanostructured photodetectors.

ACKNOWLEDGMENTS

This work was supported by the Office of Naval Research Global (award number N629092412059), and by the European Union, through two initiatives of the Italian National Recovery and Resilience Plan (NRRP) of NextGenerationEU: the PRIN Project 20225YYLEP, "Empowering UV LED technologies for high-efficiency disinfection: from semiconductor-level research to SARs-Cov-2 inactivation", and the National Centre for HPC, Big Data and Quantum Computing under Grant CN00000013 —CUP E13C22000990001. This manuscript reflects only the authors' views and opinions and the Ministry cannot be considered responsible for them.

[1] A. Rogalski, P. Martyniuk, and M. Kopytko, InAs/GaSb type-II superlattice infrared detectors: Future prospect, Appl. Phys. Rev. **4**, 031304 (2017).

[2] B. V. Olson, C. H. Grein, J. K. Kim, E. A. Kadlec, J. F. Klem, S. D. Hawkins, and E. A. Shaner, Auger recombination in long-wave infrared InAs/InAsSb type-II superlattices, Appl. Phys. Lett. **107**, 261104 (2015).

[3] A. M. Itsuno, Bandgap-engineered HgCdTe infrared detector structures for reduced cooling requirements, Ph.D. dissertation, University of Michigan, 2012.

[4] J. T. Olesberg, M. E. Flatté, T. C. Hasenberg, and C. H. Grein, Mid-infrared InAs/GaInSb separate confinement heterostructure laser diode structures, J. Appl. Phys. **89**, 3283 (2001).

[5] E. Bellotti, F. Bertazzi, A. Tibaldi, J. Schuster, J. Bajaj, and M. Reed, Disorder-induced degradation of vertical carrier transport in strain-balanced antimony-based superlattices, Phys. Rev. Appl. **16**, 054028 (2021).

[6] F. Bertazzi, A. Tibaldi, M. Goano, J. A. Gonzalez Montoya, and E. Bellotti, Non-equilibrium Green's function modeling of type-II superlattice detectors and its connection to semiclassical approaches, Phys. Rev. Appl. **14**, 014083 (2020).

[7] C. M. Ciesla, B. N. Murdin, C. R. Pidgeon, R. A. Stradling, C. C. Phillips, M. Livingstone, I. Galbraith, D. A. Jaroszynski, C. J. G. M. Langerak, P. J. P. Tang, and M. J. Pullin, Suppression of Auger recombination in arsenic-rich $InAs_{1-x}Sb_x$ strained layer superlattices, J. Appl. Phys. **80**, 2994 (1996).

[8] J. R. Meyer, C. L. Canedy, M. Kim, C. S. Kim, C. D. Merritt, W. W. Bewley, and I. Vurgaftman, Comparison of Auger coefficients in type I and type II quantum well midwave infrared lasers, IEEE J. Quantum Electron. **57**, 044045 (2021).

[9] M. Winslow, S. H. Kodati, S. Lee, D. R. Fink, T. J. Ronningen, J. C. Campbell, S. Krishna, and C. H. Grein, Simulation of impact ionization coefficients in InAlAs/InAsSb type-II superlattice material systems, J. Electron. Mater. **50**, 7293 (2021).

[10] S. Z. Ahmed, Y. Tan, J. Zheng, J. C. Campbell, and A. W. Ghosh, Atomistic transport modeling, design principles, and empirical rules for low-noise III-V digital-alloy avalanche photodiodes, Phys. Rev. Appl. **17**, 034044 (2022).

[11] S. Tempel, M. Winslow, S. H. Kodati, S. Lee, T. J. Ronningen, J. C. Campbell, S. Krishna, S. Krishnamurthy, and C. H. Grein, in *Proc. SPIE 12430* (SPIE, San Francisco, CA, USA, 2023), p. 124300G–1–20.

[12] C. H. Grein, P. M. Young, and H. Ehrenreich, Minority carrier lifetimes in ideal InGaSb/InAs superlattices, Appl. Phys. Lett. **61**, 2905 (1992).

[13] E. R. Youngdale, J. R. Meyer, C. A. Hoffman, F. J. Bartoli, C. H. Grein, P. M. Young, H. Ehrenreich, R. H. Miles, and D. H. Chow, Auger lifetime enhancement in InAs–$Ga_{1-x}In_xSb$ superlattices, Appl. Phys. Lett. **64**, 3160 (1994).

[14] C. H. Grein and H. Ehrenreich, Modeling of disorder influenced Auger recombination in strained-layer type-II superlattices, J. Appl. Phys. **93**, 1075 (2003).

[15] N. L. Bazhenov, K. D. Mynbaev, A. A. Semakova, and G. G. Zegrya, Comparative analysis of the electroluminescence efficiency in type-I and type-II heterostructures based on III-V narrow-gap compounds, Semiconductors **56**, 43 (2022).

[16] M. Isler, Phonon-assisted impact ionization of electrons in $In_{0.53}Ga_{0.47}As$, Phys. Rev. B **63**, 115209 (2001).

[17] M. Deppner, F. Römer, and B. Witzigmann, Auger carrier leakage in III-nitride quantum-well light emitting diodes, Phys. Status Solidi RRL **6**, 418 (2012).

[18] A. Tibaldi, J. A. Gonzalez Montoya, M. Vallone, M. Goano, E. Bellotti, and F. Bertazzi, Modeling infrared superlattice photodetectors: From nonequilibrium Green's functions to quantum-corrected drift diffusion, Phys. Rev. Appl. **16**, 044024 (2021).

[19] G. Alymov, V. Vyurkov, V. Ryzhii, A. Satou, and D. Svintsov, Auger recombination in Dirac materials: A tangle of many-body effects, Phys. Rev. B **97**, 205411 (2018).

[20] G. Stefanucci and R. van Leeuwen, *Nonequilibrium Many-Body Theory Of Quantum Systems. A Modern Introduction* (Cambridge University Press, Cambridge, UK, 2013).

[21] T. Schmielau and M. F. Pereira Jr., Nonequilibrium many body theory for quantum transport in terahertz quantum cascade lasers, Appl. Phys. Lett. **95**, 231111 (2009).

[22] U. Aeberhard, Quantum transport simulation of hot carrier photocurrent generation in quantum well solar cells, Semicond. Sci. Technol. **34**, 094002 (2019).

[23] L. Deuschle, J. Backman, M. Luisier, and J. Cao, in *International Conference on Simulation of Semiconductor Processes and Devices (SISPAD 2023)* (IEEE, Kobe, Japan, 2023), p. 297.

[24] S. Maimon and G. W. Wicks, *nBn* detector, an infrared detector with reduced dark current and higher operating temperature, Appl. Phys. Lett. **89**, 151109 (2006).

[25] P. Martyniuk, M. Kopytko, and A. Rogalski, Barrier infrared detectors, Opto-Electron. Rev. **22**, 127 (2014).

[26] S. Steiger, Modelling nano-LEDs, Ph.D. dissertation, Eidgenössische Technische Hochschule Zürich, 2009.

[27] U. Aeberhard, A microscopic theory of quantum well photovoltaics, Ph.D. dissertation, Eidgenössische Technische Hochschule Zürich, 2008.

[28] F. Bertazzi, M. Goano, G. Ghione, A. Tibaldi, P. Debernardi, and E. Bellotti, in *Handbook of Optoelectronic Device Modeling and Simulation*, edited by J. Piprek (CRC Press, Boca Raton, FL, 2017), chapter 2, p. 35.

[29] P. C. Klipstein, Y. Livneh, A. Glozman, S. Grossman, O. Klin, N. Snapi, and E. Weiss, Modeling InAs/GaSb and InAs/InAsSb superlattice infrared detectors, J. Electron. Mater. **43**, 2984 (2014).

[30] Y.-C. Chang and J. N. Schulman, Complex band structures of crystalline solids: An eigenvalue method, Phys. Rev. B **25**, 3975 (1982).

[31] The numerical implementation of the Bloch boundary conditions in the eigenvalue problem for the calculation of the subband structure (see, for example, [52]) is closely related with the superlattice boundary self-energy proposed here, with the propagation factors appearing in the diagonal matrices $\Lambda^{\lessgtr}$ being computed by selecting longitudinal wavenumbers k_z evenly spaced in the mini-Brillouin zone,

rather than solving for the complex band structure problem of the superlattice.

[32] D. Z. Ting, A. Soibel, and S. D. Gunapala, Hole effective masses and subband splitting in type-II superlattice infrared detectors, Appl. Phys. Lett. **108**, 183504 (2016).

[33] R. Binder and S. Koch, Nonequilibrium semiconductor dynamics, Prog. Quantum Electron. **19**, 307 (1995).

[34] J. Hader, J. V. Moloney, and S. W. Koch, Microscopic evaluation of spontaneous emission- and Auger-processes in semiconductor lasers, IEEE J. Quantum Electron. **41**, 1217 (2005).

[35] O. Bonno, J.-L. Thobel, and F. Dessenne, Modeling of electron-electron scattering in Monte Carlo simulation of quantum cascade lasers, J. Appl. Phys. **97**, 043702 (2005).

[36] U. Aeberhard, Quantum-kinetic theory of photocurrent generation via direct and phonon-mediated optical transitions, Phys. Rev. B **84**, 035454 (2011).

[37] G. G. Zegrya and A. S. Polkovnikov, Mechanisms of Auger recombination in quantum wells, J. Exp. Theor. Phys. **86**, 815 (1998).

[38] A. S. Polkovnikov and G. G. Zegrya, Auger recombination in semiconductor quantum wells, Phys. Rev. B **58**, 4039 (1998).

[39] F. Bertazzi, M. Goano, and E. Bellotti, Numerical analysis of indirect Auger transitions in InGaN, Appl. Phys. Lett. **101**, 011111 (2012).

[40] I. Vurgaftman, G. Belenky, Y. Lin, D. Donetsky, L. Shterengas, G. Kipshidze, W. L. Sarney, and S. P. Svensson, Interband absorption strength in long-wave infrared type-II superlattices with small and large superlattice periods compared to bulk materials, Appl. Phys. Lett. **108**, 222101 (2016).

[41] E. H. Aifer, J. G. Tischler, J. H. Warner, I. Vurgaftman, W. W. Bewley, J. R. Meyer, J. C. Kim, L. J. Whitman, C. L. Canedy, and E. M. Jackson, W-structured type-II superlattice long-wave infrared photodiodes with high quantum efficiency, Appl. Phys. Lett. **89**, 053519 (2006).

[42] M. Razeghi, *Fundamentals of Solid State Engineering* (Springer, Evanston, IL, 2009), 3rd ed.

[43] M. Razeghi and B.-M. Nguyen, Band gap tunability of type II antimonide-based superlattices, Phys. Procedia **3**, 1207 (2010).

[44] D. Z. Ting, A. Khoshakhlagh, A. Soibel, and S. D. Gunapala, Long wavelength InAs/InAsSb infrared superlattice challenges: A theoretical investigation, J. Electron. Mater. **49**, 6936 (2020).

[45] J. R. Meyer, C. A. Hoffman, F. J. Bartoli, and L. R. Ram-Mohan, Type-II quantum-well lasers for the mid-wavelength infrared, Appl. Phys. Lett. **67**, 757 (1995).

[46] B.-M. Nguyen and M. Razeghi, in *Proc. SPIE 6479* (SPIE, San Jose, CA, USA, 2007), p. 86191J.

[47] P. C. Klipstein, Y. Benny, Y. Cohen, N. Fraenkel, S. Gliksman, A. Glozman, I. Hirsh, L. Langof, I. Lukomsky, I. Marderfeld, B. Milgrom, M. Nitzani, D. Rakhmilevich, L. Shkedy, N. Snapi, I. Shtrichman, E. Weiss, and N. Yaron, Performance limits of III-V barrier detectors, J. Electron. Mater. **49**, 6893 (2020).

[48] J. Hader, J. V. Moloney, and S. W. Koch, Supression of carrier recombination in semiconductor lasers by phase-space filling, Appl. Phys. Lett. **87**, 201112 (2005).

[49] J. R. Meyer, C. L. Felix, W. W. Bewley, I. Vurgaftman, E. H. Aifer, L. J. Olafsen, J. R. Lindle, C. A. Hoffman, M.-J. Yang, B. R. Bennett, B. V. Shanabrook, H. Lee, C.-H. Lin, S. S. Pei, and R. H. Miles, Auger coefficients in type-II $InAs/Ga_{1-x}In_xSb$ quantum wells, Appl. Phys. Lett. **73**, 2857 (1998).

[50] I. Vurgaftman, W. W. Bewley, C. L. Canedy, C. S. Kim, M. Kim, C. D. Merritt, J. Abell, and J. R. Meyer, Interband cascade lasers with low threshold powers and high output powers, IEEE J. Select. Topics Quantum Electron. **19**, 1200210 (2013).

[51] I. Vurgaftman, W. W. Bewley, C. L. Canedy, C. S. Kim, M. Kim, C. D. Merritt, J. Abell, J. R. Lindle, and J. R. Meyer, Rebalancing of internally generated carriers for mid-infrared interband cascade lasers with very low power consumption, Nat. Commun. **2**, 585 (2011).

[52] P.-F. Qiao, S. Mou, and S. L. Chuang, Electronic band structures and optical properties of type-II superlattice photodetectors with interfacial effect, Opt. Express **20**, 2319 (2012).